Early Paleozoic slab rollback in the North Altun, Northwest China: New evidence from ma□c intrusions and high-Mg andesites

Xian-Tao Ye[1], Chuan-Lin Zhang[1], Ai-Guo Wang[2], Bin Wu[2], and Guo-Dong Wang[3]

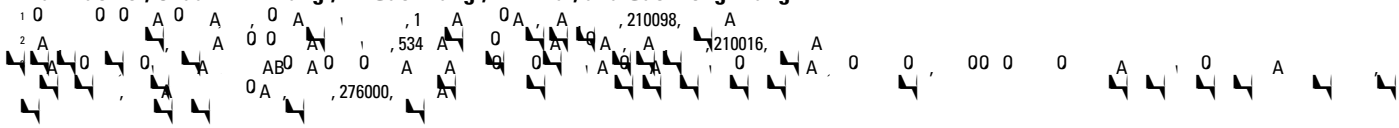

ABSTRACT

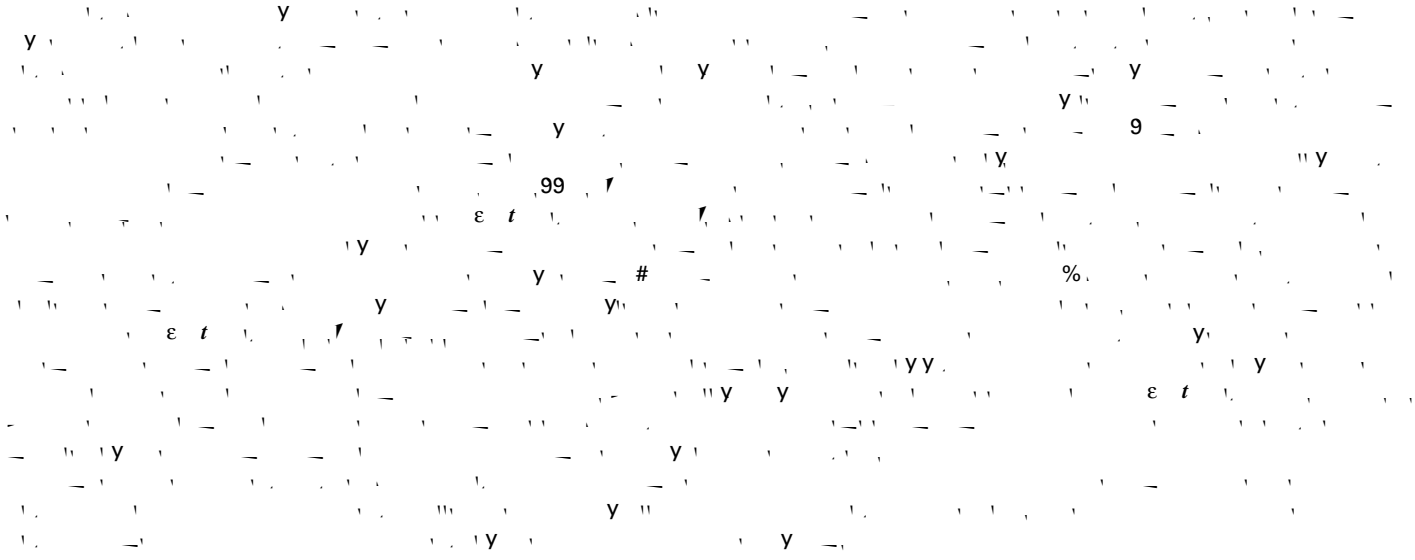

2018355 2018 /10.1130/ 732.1

INTRODUCTION

The Altun orogen is located at the northern margin of the Qinhai-Tibet Plateau (Fig. 1A; Wu et al., 2006, 2009; Xu et al., 1999, 2011). Recent studies show that the Altun orogen is a composite orogenic belt, consisting of microcontinents and multiple ophiolite and high-pressure to ultrahigh-pressure metamorphic belts (Xu et al., 1999; Zhang et al., 2005b). In spite of many studies in the area, its Paleozoic tectonic evolution has remained equivocal (Cowgill et al., 2003; L. Liu et al., 1997, 2007; Sobel and Arnaud, 1999; Wu et al., 2006, 2016; J.X. Zhang et al., 2005a, 2005b; Z.C. Zhang et al., 2010b).

Based on the age of the high-pressure and low-temperature (HP/LT) metamorphic rocks in the North Altun, Zhang et al. (2007) suggested that slab subduction began ca. 520 Ma. This is consistent with the presence of arc-related granitic rocks and the occurrence of early Paleozoic ophiolites in the belt (Gai et al., 2015; Gao et al., 2012; Yang et al., 2008). However, the tectonic evolution of this area was divided into different stages by previous scholars (e.g., Han et al., 2012; Liu et al., 2016; Meng et al., 2017). In addition, the early Paleozoic tectonic evolution, especially the subduction history of the belt, has not yet been characterized (Meng et al., 2017).

Mafic rocks are known to occur in the North Altun (Xinjiang BGMR, 1981, 2006), but little is known about their geochronology or petrogenesis or their relationship with the widespread silicic magmatism. Mafic rocks have different geochemical features that result from the different tectonic settings in which they formed. These features can also be used to constrain the nature of the mantle source (Hollanda et al., 2006; Yang and Zhou, 2009), the extent of metasomatism by subduction-related materials (Kepezhinskas et al., 1997), and the degree of interaction between mantle-derived magmas and crustal materials (DePaolo, 1981). Therefore,

In this study, we report detailed field observations, petrography, ages, and comprehensive geochemistry analyses of the mafic intrusions and andesitic lavas occurring in the volcanic-sedimentary sequence in the Kaladawan area at the northern margin of the Altun orogen. The main objectives of this study were to: (1) refine the previously invoked tectonic model based on the distinct metamorphism and multiphase emplacement of the ophiolites, and (2) elucidate the subduction/collision-induced extension in the Altun orogenic belt.

REGIONAL GEOLOGY

The Altun orogen lies between the Tarim Basin to the north and the Qaidam Basin, Kunlun Mountains, and Tibetan Plateau to the south (Fig. 1A). From north to south, the Altun orogen can be divided into four tectonic units: the North Altun Archean complex (or the Dunhuang block), the North Altun oceanic subduction-collision complex, the Central Altun block (also known as the Milanhe-Jinyanshan block), and the South Altun continental-type subduction-collision complex (Fig. 1B; L. Liu et al., 2007, 2009, 2012; Wu et al., 2009; Zhang et al., 2014). The North Altun subduction complex consists of early Paleozoic volcanic-sedimentary sequences, ophiolites, high-pressure metamorphic rocks, and various granitic rocks. The volcanic-sedimentary sequence is termed the Lapeiquan Formation (or Kaladawan Formation; Xinjiang BGMR, 2006), outcropping extensively

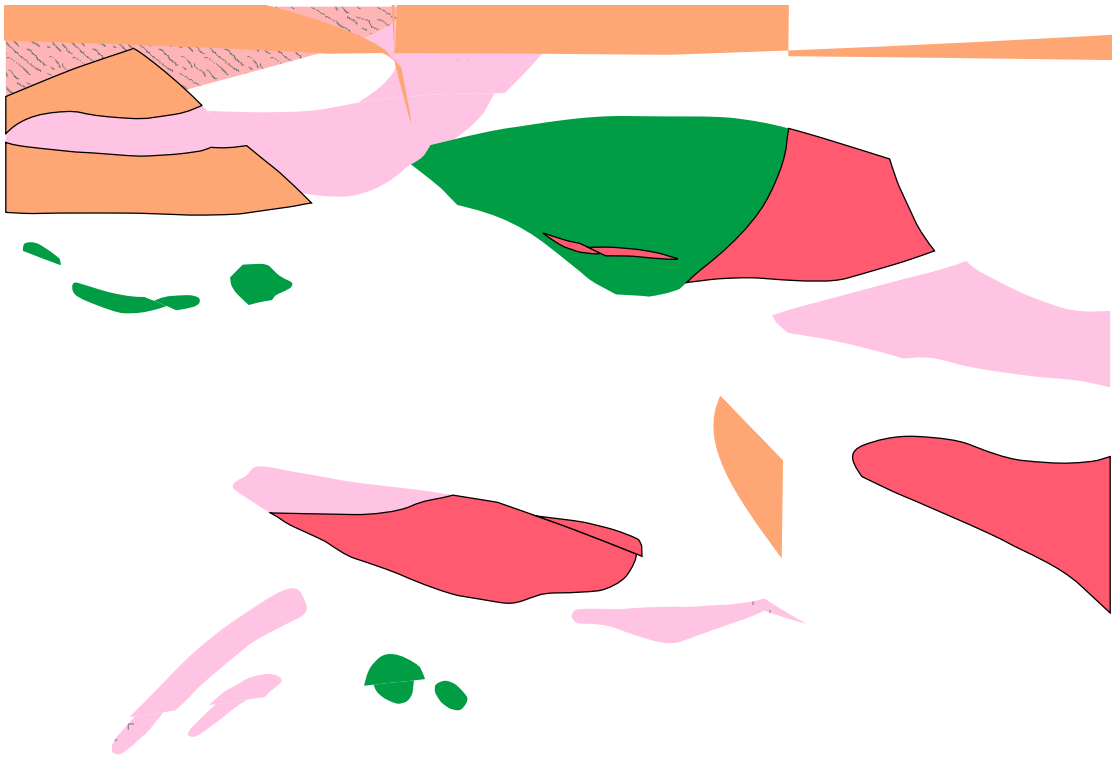

eclogites formed during 510–490 Ma (Zhang and Meng, 2006; J.X. Zhang et al., 2005b, 2007, 2010). Granitoids can be subdivided into two groups: 520–470 Ma subduction-related I-type granites (Han et al., 2012; Kang et al., 2011; C. Liu et al., 2016; J.H. Liu et al., 2017; Wu et al., 2006) and 440–410 Ma I- and S-type anorogenic granites (Chen et al., 2003, 2009; Han et al., 2012; Z.C. Zhang et al., 2010b). Based on the presence of HP/LT metamorphic assemblages, and ophiolitic, subduction-accretion complex, and arc magmatic rocks, Zhang et al. (2015) proposed that the North Altun could be considered as a typical early Paleozoic accretionary orogenic belt.

Compared to the extensive distribution of granitoids along the North Altun, rare gabbroic intrusions occurred in this area. These intrusions form an E-W–trending belt from Hongliugou to Lapeiquan (Fig. 1C). The Kaladawan area, located in the eastern North Altun, hosts the Lapeiquan Formation, granitoids, and several mafic intrusions (Dawan and Dabanxi intrusions) and the Dawan mafic dikes. However, the emplacement ages, petrogenesis, and tectonic regime of these mafic rocks remain unknown.

FIELD OBSERVATION AND SAMPLE COLLECTION

Lapeiquan Formation

The Lapeiquan Formation is divided into lower and upper sections, outcropping along the Hongliugou-Lapeiquan ophiolite belt (Figs. 2 and 3A). The Lapeiquan Formation unconformably overlies the Neoproterozoic Muzisayi Formation. At its southern margin, it connects with the Paleogene Gancaigou Formation by a thrust fault. The lower section of the Lapeiquan Formation consists mainly of layers of mafic to silicic volcanic and volcaniclastic rocks, including basalt, andesite, dacite, rhyolite, and sericite-chlorite (quartz) schist (Fig. 3B; Ni et al., 2017; Xinjiang BGMR, 2006). In addition, it hosts a massive iron-ore deposit (Qi et al., 2008). The upper section of the Lapeiquan Formation is composed chiefly of clastic rocks, interbedded with minor metavolcanics and carbonates (Fig. 3C). It underwent lower-greenschist-facies metamorphism and tightly folded deformation. The upper Lapeiquan Formation sedimentary sequence extends more than 100 km from Qiongtage to the Lapeiquan area. Field and thin section observations have revealed that the major rock types are sericite-chlorite (quartz) schist, fine-grained sandstone, rhyolite, phyllite, ignimbrite, and dolomite. Lower-greenschist-facies metamorphic minerals such as biotite, sericite, and chlorite are commonly seen in most rock types. It should be noted that the upper Lapeiquan Formation hosts a large Pb-Zn-Ag-Cu polymetallic ore deposit in this region.

One rhyolite sample from the lower Lapeiquan Formation (16AB02: 39°07′14″N, 91°37′51″E; Fig. 4A) and two rhyolite samples from the upper Lapeiquan Formation (1101: 39°03′40″N, 91°37′51″E and 1106: 39°07′14″N, 91°37′51″E; Fig. 4B) were collected for zircon U-Pb dating. Ten andesitic samples (39°05′22″N, 91°44′55″E) were collected for

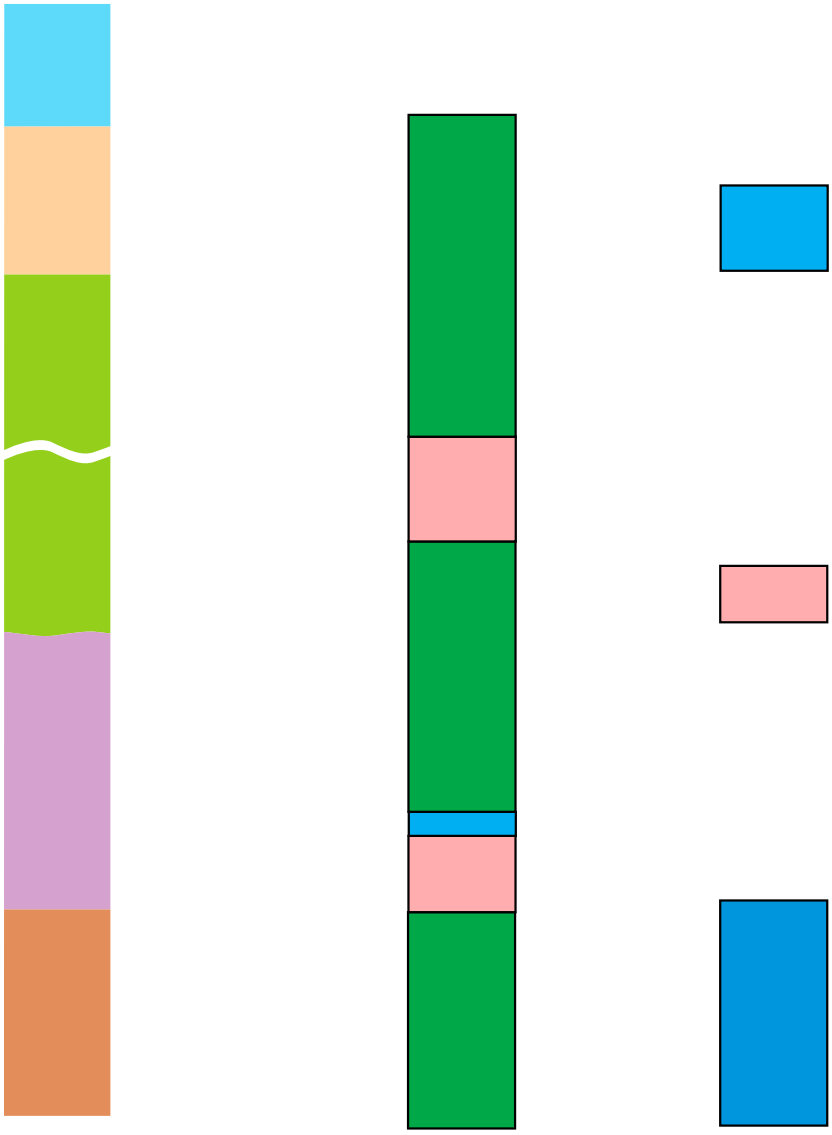

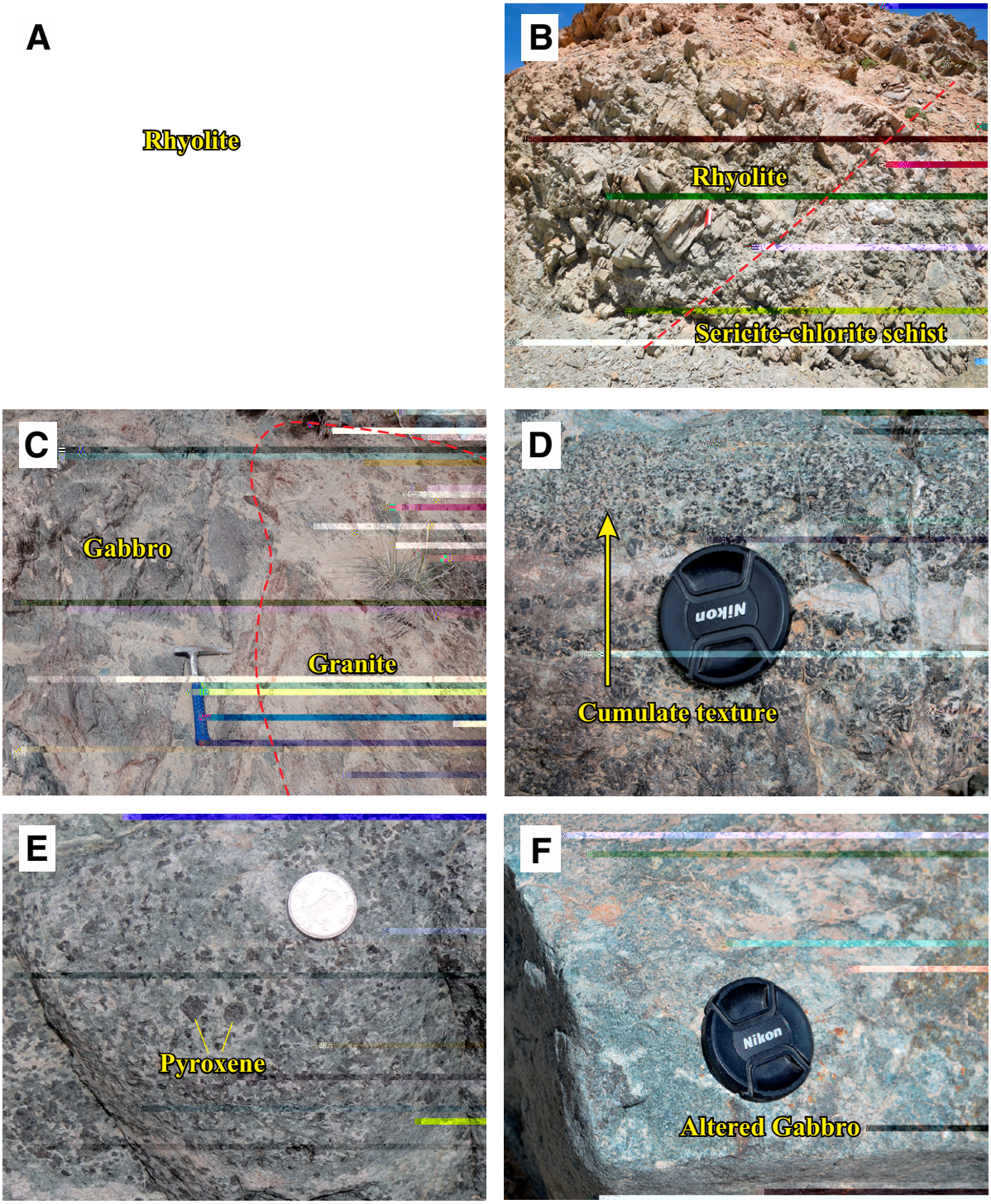

Figure 4. Field photographs of the Dawan mafic intrusion, rhyolite from the lower and upper Lapeiquan Formation, and the Dabanxi mafic intrusion: (A) cumulate structure of the Dawan gabbros; (B) euhedral pyroxenes in the Dawan gabbros; (C) intrusive contact between the Dawan mafic intrusion and granitic rocks; (D) interbedded rhyolite layer from the lower Lapeiquan Formation; (E) relationship between the rhyolite and sericite-chlorite schist from the upper Lapeiquan Formation; and (F) alteration of gabbro from the Dabanxi mafic intrusion.

geochemical work. Rhyolites have euhedral to subhedral crystal plagioclase and potassium feldspar (K-feldspar; Figs. 5A and 5B), whereas andesites contain plagioclase (30%–45%), hornblende (40%–45%), K-feldspar (5%–10%), quartz (5%–10%), and minor epidote, zircon, and apatite (Fig. 5C).

Dawan Intrusion

The Dawan gabbroic intrusion is one of the largest mafic intrusions in the Kaladawan area. It shares a fault contact with country rocks (Xinjiang BGMR, 2006), and then is intruded by a granitic pluton (Fig. 4C). Massive structure and cumulate texture are evident. Rhythmic layering of plagioclase and pyroxene is commonly observed at several outcrops in the field (Fig. 4D). The gabbro has typical gabbroic texture with euhedral to semi-euhedral pyroxene and plagioclase in both outcrop and thin sections (Figs. 4E, 5D, and 5E). The main minerals are clinopyroxene (40%–50%) and plagioclase (30%–45%). The minor minerals include hornblende and epidote. Zircon, titanite, and apatite are present as accessory minerals. One geochronological sample (16DW02: 39°08′08″N, 91°43′19″E) and seven geochemical samples were collected from this pluton. In addition, one sample from the granitic pluton intruding the gabbro (AYT001: 39°08′31″N, 91°42′5″E) was collected for geochronological analysis.

Dabanxi Intrusion

In the Kaladawan area, dozens of E-W–trending mafic intrusions and dikes were emplaced in the lower Lapeiquan Formation (Fig. 2). Among them, the Dabanxi intrusion, of coarse-grained texture and with a total outcrop area of ~1 km^2, is relatively suitable for zircon selection.

The dominant rocks of the Dabanxi stocks are coarse- to medium-grained gabbros (Fig. 4F). The gabbros are generally composed of euhedral crystals of plagioclase and clinopyroxene, with minor hornblende, biotite, apatite, and Fe-Ti oxides. Most of the gabbros have experienced

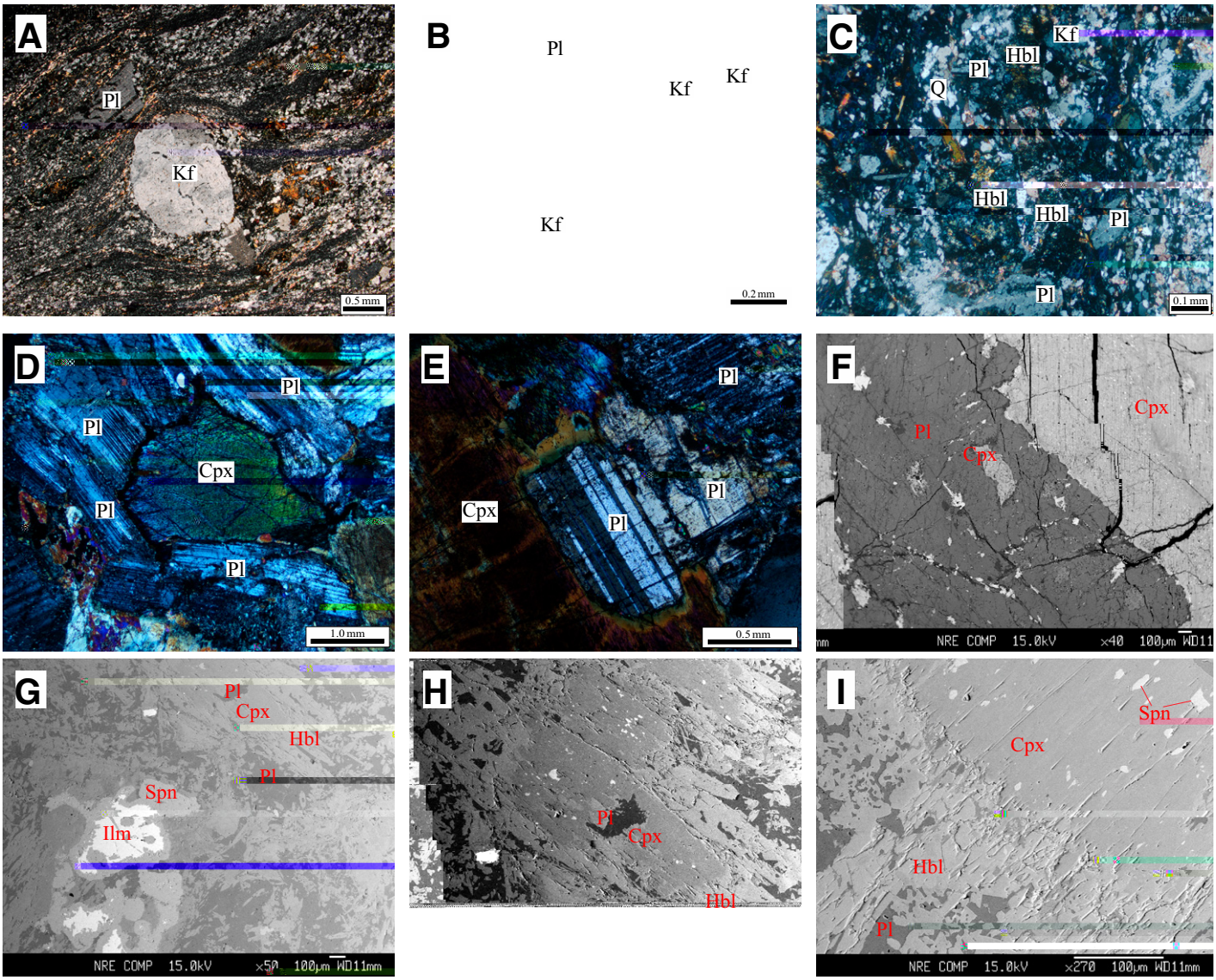

Figure 5. Photomicrographs of: (A, B, C) Dawan gabbros, (D) rhyolite from the lower Lapeiquan Formation, (E) rhyolite from the upper Lapeiquan Formation, (F) andesite from the lower Lapeiquan Formation, and (G, H, I) Dabanxi gabbros (see details in the text). Cpx—clinopyroxene; Hbl—hornblende; Ilm—ilmenite; Kf—K-feldspar; Pl—plagioclase; Q—quartz; Spn—sphene.

variable degrees of alteration, resulting in albitization of some plagioclases and some alteration of clinopyroxene to amphibole, chlorite, or epidote (Fig. 5G). In thin section, the gabbro contains 40%–50% plagioclase and 45%–50% clinopyroxene, with minor hornblende, epidote, sphene, and Fe-Ti oxides (Figs. 5H and 5I). One sample for geochronology (16DBX04: 39°04′19″N, 91°41′55″E) and 10 samples for geochemical analyses were collected from this intrusion.

ANALYTICAL METHODS

Zircon separation was carried out using conventional heavy liquid and magnetic separation techniques. Zircon grains were then handpicked under a binocular microscope, and representative grains and zircon standards (TEMORA) were mounted in epoxy resin disks. These were then polished to approximately half their thickness. Zircons were photographed under transmitted and reflected light, and cathodoluminescence (CL) images were taken to reveal their internal structures.

Zircon U-Pb analyses were carried out using sensitive high-resolution ion microprobe II (SHRIMP II) and laser ablation–inductively coupled plasma–mass spectrometry (LA-ICP-MS) techniques at the Beijing SHRIMP Center, Chinese Academy of Geological Sciences, and Tianjin Institute of Geology and Mineral Resources, respectively. Ion microprobe procedures followed those described by Williams (1998), whereas LA-ICP-MS analytical procedures were described by Geng et al. (2011) and Hou et al. (2009). Data reduction was performed off-line using ICPMS-DataCal (Liu et al., 2010a, 2010b). SQUID 1.0 and Isoplot (Ludwig, 1999) software were used for data processing. Zircon U-Pb age data are listed in Table DR1 in the GSA Data Repository Item.[1]

Clinopyroxene compositions were determined by wavelength-dispersion X-ray emission spectrometry using a JEOL JXA-8100 electron-probe microanalyzer (EMPA) at the State Key Laboratory Breeding Base of Nuclear Resources and Environment, Nanchang, China. Operating conditions were 15 kV accelerating voltage and 20 nA beam current, with a 10 s counting time. Representative mineralogical data are listed in Tables DR2 and DR3 in the GSA Data Repository Item.

Major elements were measured by using a Rigaku ZSX100e X-ray fluorescence spectrometer (XRF) at the State Key Laboratory of Ore Deposit Geochemistry, Institute of Geochemistry, Chinese Academy of Sciences (CAS). Whole-rock samples were crushed and powdered to less than 200 mesh in an agate mill, and then samples were fused with lithium-tetraborate glass pellets. Analytical precision as determined by Chinese National Standards GSR-1 and GSR-3 was generally ~1%–5%. Trace elements were analyzed using a Perkin-Elmer ELAN-DRC-e ICP-MS at the State Key Laboratory of Ore Deposit Geochemistry, Institute of Geochemistry, CAS. Powdered samples (50 mg) were digested in high-pressure Teflon bombs using an HF + HNO_3 mixture for 48 h at ~195 °C (Qi et al., 2000). Analytical precision for most elements was better than 3%–5%. Analytical results are presented in Table 1.

Samples for Nd-Sr isotopic measurement were spiked and dissolved in Teflon bombs with HF + HNO_3 acid and then separated by conventional cation-exchange techniques. The isotopic measurements were performed on a Thermo Fisher Triton TI thermal ionization mass spectrometer (TIMS) at the State Key Laboratory of Ore Deposit Geochemistry, Institute of Geochemistry, CAS. The detailed procedure we used is as described by Li et al. (2004). Measured $^{87}Sr/^{86}Sr$ and $^{143}Nd/^{144}Nd$ ratios were corrected to $^{86}Sr/^{88}Sr = 0.1194$ and $^{146}Nd/^{144}Nd = 0.7219$, respectively. The reported $^{87}Sr/^{86}Sr$ average ratios for the NBS987 standard and BCR-2 standard were $^{87}Sr/^{86}Sr = 0.710219 \pm 5$ (2σ) and 0.704966 ± 3 (2σ), respectively, and the $^{143}Nd/^{144}Nd$ average ratios for the LRIG and BCR-2 standards were $^{143}Nd/^{144}Nd = 0.512196 \pm 3$ (2σ) and 0.512634 ± 4 (2σ), respectively. Analytical results and calculated parameters are listed in Table 2.

ANALYTICAL RESULTS

Zircon U-Pb Ages

Dawan Intrusion (Gabbroic Sample 16DW02 and Granitic Sample AYT001)

Zircons in sample 16DW02 are euhedral, with average crystals size up to 50–80 μm and length-to-width ratios from 1:1 to 2:1. All zircons are colorless and without obvious zoning (Fig. 6). Fifteen grains were analyzed in this sample. Among them, five spots yielded younger ages, ranging from 222 to 406 Ma, which may reflect the effects of alteration and/or metamorphic events after emplacement, due to the absence of clear oscillatory growth zoning and presence of white or dark areas in their CL images. The other 10 spots have U and Th contents of 338–2989 ppm and 178–1678 ppm, respectively, with Th/U ratios varying from 0.11 to 0.91 (Table DR1). Most zircons show variable discordance between $^{206}Pb/^{238}U$ and $^{207}Pb/^{235}U$ ages but yield a discordance line with an intercept age of 524 ± 22 Ma (mean square of weighted deviates [MSWD] = 0.27; Fig. 7A). On the other hand, their $^{206}Pb/^{238}U$ ages are consistent within error and yield a weighted mean age of 515 ± 9 Ma (Fig. 7A), which is comparable to the intercept age.

Zircons from sample AYT001 are broadly euhedral (Fig. 6), with length ranging from 80 to 100 μm, and length-to-width ratio of 2:1. Thirty-two grains were analyzed on 32 grains. The data show variable U (275–1665 ppm) and Th (76–999 ppm) contents, with Th/U ratios of 0.28–0.96 (Table DR1). Excepting spots 07, 09, and 20, the other analyses define a good discordia with upper intercept age of 510 ± 3 Ma (MSWD = 0.54), and a weighted mean $^{206}Pb/^{238}U$ age of 511 ± 2 Ma (MSWD = 0.53; Fig. 7B).

Lapeiquan Formation (Rhyolites 16AB02, 1101, and 1106)

Zircons in sample 16AB02 are transparent, euhedral prismatic grains with concentric zoning in CL images (Fig. 6), and they are ~80 μm in length with aspect ratios of 1:1 to 2:1. Fifteen grains were analyzed, which yielded variable U and Th contents (U = 254–525 ppm, Th = 109–345 ppm, Th/U = 0.42–0.69). All analyses were concordant within analytical errors and yielded a weighted mean $^{206}Pb/^{238}U$ age of 495 ± 4 Ma (MSWD = 0.45; Fig. 7C).

Zircons from samples 1101 and 1106 are transparent and pinkish in color, range from 100 to 150 μm in length, and have length-to-width ratios of 2:1 to 3:1. In CL images, interval growth zoning is clear in most of the zircon crystals, and no core-rim structure is observed (Fig. 6). In total, 32 analyses on sample 1101 showed that the concentrations of U and Th are in the ranges of 401–987 ppm and 161–445 ppm, respectively, with consistent Th/U ratios between 0.37 and 0.60 (Table DR1). The measured $^{206}Pb/^{238}U$ ages are in good agreement within analytical error and yield a weighted mean age of 484 ± 2 Ma (MSWD = 0.78; Fig. 7D). Sample 1106 has variable contents of U (250–2007 ppm) and Th (74–1103 ppm), with Th/U ratios of 0.30–0.85 (Table DR1). All 32 analyses form a tight cluster on a concordia plot and yield a weighted mean $^{206}Pb/^{238}U$ age of 488 ± 2 Ma (MSWD = 0.36; Fig. 7E).

[1] 2018355, 1: (16 02, 16AB02, 16 B 04) A- , - (A 001, 1101, 1106) ; 2: ; 3: ://... /2018, ...

TABLE 1. GEOCHEMICAL COMPOSITIONS OF THE DAWAN INTRUSION, DAWAN HIGH-Mg ANDESITES, AND DABANXI INTRUSION

Site	Dawan intrusion						Dawan high-Mg andesites										Dabanxi intrusion									
Rock	Gabbro	Gabbro	Gabbro	Gabbro	Gabbro	Gabbro	Andesite	Andesite	Andesite	Andesite	Andesite	Andesite	Andesite	Andesite	Andesite	Andesite	Gabbro	Gabbro	Gabbro	Gabbro	Gabbro	Gabbro	Gabbro	Gabbro	Gabbro	Gabbro
Sample	AYT002 H1	AYT002 H2	AYT002 H3	AYT002 H5	AYT002 H6	AYT002 H7	AYT004 H1	AYT004 H2	AYT004 H3	AYT004 H4	AYT004 H5	AYT004 H6	AYT004 H7	AYT004 H8	AYT004 H9	AYT004 H10	AYT006 H1	AYT006 H2	AYT006 H3	AYT006 H4	AYT006 H5	AYT006 H6	AYT006 H7	AYT006 H8	AYT006 H10	AYT006 H10
SiO_2	48.1	45.8	47.6	47.5	49.1	50.0	55.4	55.9	54.7	52.9	54.6	58.0	57.1	58.1	58.7	57.8	47.4	46.7	46.1	45.8	44.5	45.8	45.3	46.9	47.6	47.6
TiO_2	0.25	0.69	0.25	0.21	0.47	0.20	0.610	0.65	0.57	0.58	0.65	0.92	1.14	0.95	0.98	0.91	1.01	0.88	0.94	1.00	1.00	0.90	0.97	0.92	1.52	1.56
Al_2O_3	17.6	15.6	15.9	19.5																						

TABLE 2. Sr-Nd ISOTOPIC COMPOSITIONS OF THE MAFIC ROCKS AND ANDESITES

Sample	Rock type	Rb (ppm)	Sr (ppm)	$^{87}Rb/^{86}Sr$	$^{87}Sr/^{86}Sr$ (2σ)	$(^{87}Sr/^{86}Sr)_i$	Sm (ppm)	Nd (ppm)	$^{147}Sm/^{144}Nd$	$^{143}Nd/^{144}Nd$ (2σ)	$(^{143}Nd/^{144}Nd)_i$	$\varepsilon_{Nd}(t)$
Dawan intrusion												
AYT002H1	Gabbro	14.31	179	0.2313	0.706078 (22)	0.70438	0.55	1.42	0.2342	0.513141 (18)	0.5123508	7.4
AYT002H2	Gabbro	16.74	140	0.3460	0.707840 (11)	0.70530	1.51	4.26	0.2143	0.512989 (16)	0.5122664	5.7
AYT002H5	Gabbro	2.73	205	0.0385	0.705630 (12)	0.70535	0.43	1.18	0.2198	0.513078 (14)	0.5123366	7.1
AYT002H6	Gabbro	9.27	201	0.1334	0.705600 (9)	0.70462	1.52	4.45	0.2065	0.512700 (18)	0.5120032	0.6
Dawan high-Mg andesites												
AYT004H2	Andesite	109.80	249	1.2775	0.720697 (7)	0.71169	2.39	11.1	0.1302	0.512235 (19)	0.5118131	–3.7
AYT004H6	Andesite	59.31	257	0.6685	0.719358 (11)	0.71464	3.87	16.7	0.1401	0.512156 (21)	0.5117014	–5.8
Dabanxi intrusion												
AYT006H1	Gabbro	16.29	261	0.1806	0.707051 (7)	0.70587	2.21	7.07	0.1890	0.512825 (27)	0.5122551	4.1
AYT006H6	Gabbro	15.84	248	0.1848	0.707204 (7)	0.70599	1.82	6.03	0.1825	0.512626 (24)	0.5120757	0.6
AYT006H10	Gabbro	8.22	255	0.0932	0.708039 (6)	0.70743	2.94	9.92	0.1792	0.512732 (26)	0.5121918	2.9

Note: Chondritic uniform reservoir (CHUR) values ($^{87}Rb/^{86}Sr$ = 0.0847, $^{87}Sr/^{86}Sr$ = 0.7045; $^{147}Sm/^{144}Nd$ = 0.1967, $^{143}Nd/^{144}Nd$ = 0.512638) were used for the calculation. $\lambda_{Sm} = 6.54 \times 10^{-12}$ yr^{-1} (Lugmair and Harti, 1978). The $(^{87}Sr/^{86}Sr)_i$, $(^{143}Nd/^{144}Nd)_i$, and $\varepsilon_{Nd}(t)$ values of samples AYT002, AYT006, and AYT004 were calculated using ages of 515 Ma, 460 Ma, and 495 Ma, respectively. The two-stage model age (T_{2DM}) calculations may be found in Jahn et al. (1999).

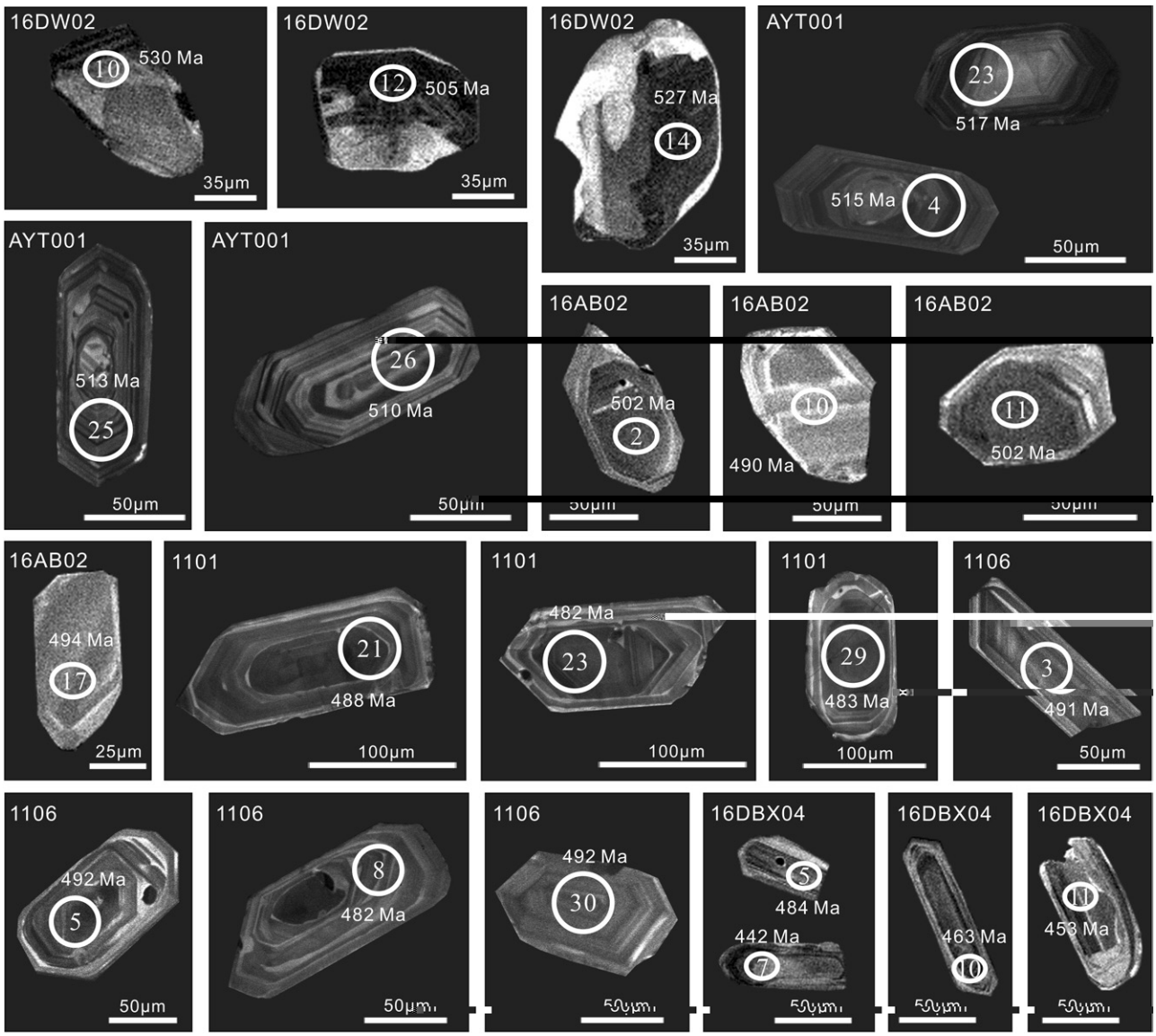

Figure 6. Representative cathodoluminescence (CL) images of zircon from the Dawan mafic intrusion, rhyolites from the lower and upper Lapeiquan Formation, and the Dabanxi mafic intrusion. Analytical spots and ages are shown (see details in the text).

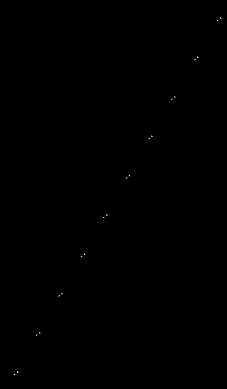

Dabanxi Intrusion (Gabbroic Sample 16DBX04)

Zircons from sample 16DBX04 are transparent and are 50–150 µm in length, with length-to-width ratios between 1:1 and 3:1. Most zircons are prismatic crystals without obvious zoning in CL images (Fig. 6). Fifteen analyses were conducted on 15 zircons (Table DR1). Among them, nine analyses showed variable levels of U and Th, from 277 ppm to 947 ppm and from 96 ppm to 614 ppm, respectively, with Th/U ratios between 0.26 and 0.98. These nine analyses have concordant U-Pb ages and show a tight group, yielding a weighted mean $^{206}Pb/^{238}U$ age of 460 ± 14 Ma (MSWD = 6.9), which is interpreted as the crystallization age of the Dabanxi intrusion (Fig. 7F). Two analyses (spot-4 and spot-6) give slightly older $^{206}Pb/^{238}U$ ages from 545 Ma to 514 Ma (Table DR1). Results from another four spots (spot-2, spot-8, spot-9, and spot-12) give younger $^{206}Pb/^{238}U$ ages from 423 Ma to 296 Ma, with higher common Pb than the others, suggesting that the U-Pb isotopic system might have been modified during postemplacement alteration.

Mineral Chemical Compositions

Nineteen clinopyroxene grains from the Dawan gabbros have SiO_2 contents between 48.90 and 52.70 wt%, CaO between 22.04 and 25.02 wt%, TiO_2 between 0.15 and 1.07 wt%, FeO between 4.98 and 6.17 wt%, and Na_2O in the range of 0.26–0.84 wt%. Calculations using Minpet (version 2.02) indicated that the clinopyroxenes exhibit high Mg# (82–85). These clinopyroxenes are characterized by high Ca and low Ti, Al, and Na, and they plot in the diopside field in the Wo-En-Fs diagram (Fig. 8A), resembling clinopyroxenes from Alaskan-type complexes (Snoke et al., 1981; Helmy and El Mahallawi, 2003; Ye et al., 2015). Furthermore, they define a clear arc cumulate trend in the Al^{VI} versus TiO_2 diagram (Figs. 8B and 8C; after Loucks, 1990).

Thirty-seven clinopyroxene grains from the Dabanxi gabbros were analyzed for chemical compositions (Table DR3). They have relative high SiO_2 (50.56–54.29 wt%) and Al_2O_3 (2.85–6.87 wt%) contents, low MgO (14.58–18.03 wt%), CaO (12.84–14.24 wt%), and TiO_2 (0–0.25 wt%) contents, and Mg# ranging from 66 to 78. They plot in the field of augite in the Wo-En-Fs diagram (Fig. 8A) and show arc-related features according to their SiO_2, Al_2O_3, and TiO_2 contents (Figs. 8B and 8C).

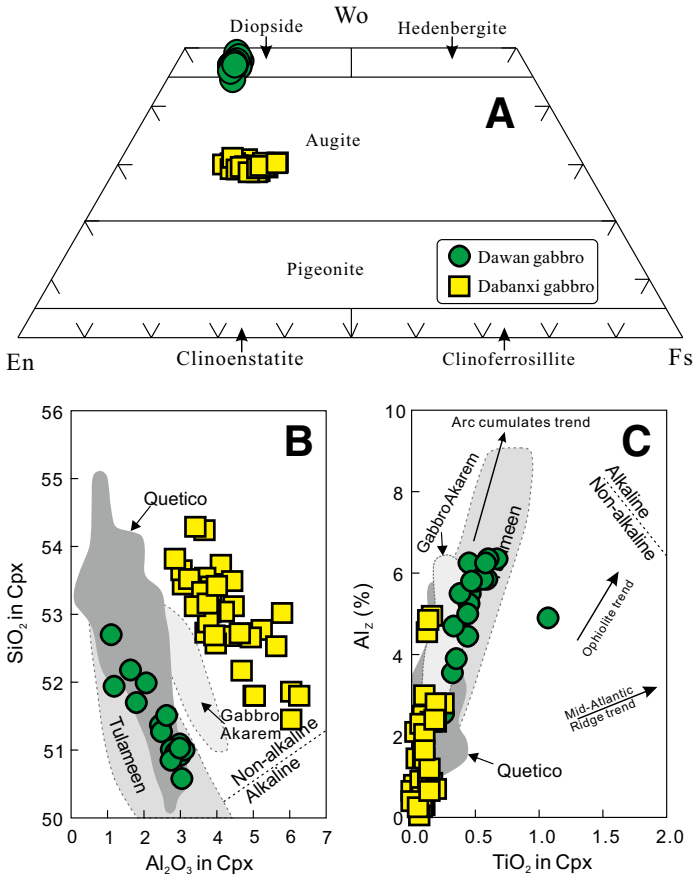

Figure 8. (A) Wo-En-Fs diagram showing the compositions of the clinopyroxene from the Dawan intrusion; (B) Al_2O_3 (wt%) vs. SiO_2 (wt%) and (C) TiO_2 (wt%) vs. Al^{IV} (percentage of tetrahedral site occupied by Al_2) in clinopyroxene from the Dawan intrusion. Gray fields are modified from Ye et al. (2015); reference lines of arc-related and rift-related tectonic environments are from Loucks (1990).

Whole-Rock Elemental Geochemistry

Seven gabbro samples from the Dawan intrusion, 10 andesite samples from the lower Lapeiquan Formation, and 10 gabbro samples from the Dabanxi intrusion were collected for major- and trace-element analyses (Table 1). The concentrations of major oxides, described below in weight percent, were recalculated to 100% on a volatile-free base.

All studied samples have undergone varying degrees of alteration, consistent with the observed fluctuation in loss on ignition (LOI) values (1.27–6.66 wt%). Thus, evaluation is required to assess the effects of alteration on the chemical compositions of these samples. Zirconium is conventionally regarded as an immobile element during low- to medium-grade alteration in igneous rocks (e.g., Wood et al., 1979). Therefore, a number of elements with different geochemical behaviors (e.g., Rb, Sr, Ba, Nb, La, Y, Th, U, and Ti) were plotted against Zr to evaluate their mobility during alteration (e.g., Fan et al., 2013). High field strength elements (HFSEs; Nb, Th, and Y), rare earth elements (REEs), U, and siderophile elements (such as Ti) showed strong correlations with Zr. In contrast, some large ion lithophile elements (LILEs; Rb, Sr, and Ba) were scattered over the plots (figure not shown). Consequently, mobile elements such as Rb, Sr, and Ba, and Sr isotopic compositions cannot be used in the geochemical classification and petrogenetic discussion.

Dawan Intrusion

Gabbros from the Dawan intrusion have SiO_2 contents ranging from 47.2 to 51.9 wt% and display variable levels of $Fe_2O_3^T$ (4.54–7.52 wt%), Al_2O_3 (16.1–20.5 wt%), CaO (11.3–16.9 wt%), TiO_2 (0.21–0.71 wt%), Na_2O (1.22–2.24 wt%), and K_2O (0.11–1.02 wt%), owing to crystal fractionation/cumulation effects (Table 1). The gabbro samples plot in the subalkaline field of the total alkali-silica (TAS) diagram (figure not shown) and define a typical tholeiitic trend in the TiO_2 versus FeO^{total}/MgO diagram (Fig. 9B).

The Dawan gabbros contain variable compatible element contents, e.g., Cr ranges from 334 to 1080 ppm, Ni ranges from 125 to 153 ppm, and V ranges from 104 to 209 ppm, due to crystal fractionation/cumulation. On the other hand, they have low total REE contents between 7.0 and 24.3 ppm (Table 1). The gabbros mostly show flat chondrite-normalized REE patterns, with $(La/Yb)_N$ ranging from 0.99 to 1.07 (Fig. 10A). Significant positive Eu anomalies (δEu = 1.5–1.9) are observed in several samples (AYT002H1, AYT002H3, AYT002H5, AYT002H7), yet another two (AYT002H2 and AYT002H6) show no obvious Eu anomalies (δEu = 0.99–1.07; Fig. 10A). Normalized to primitive mantle, all samples exhibit variable enrichments in LILEs and pronounced Nb depletion (Nb/La = 0.13–0.80; Fig. 10B). The positive Sr anomalies are concurrent with the positive Eu anomalies, indicating plagioclase accumulation.

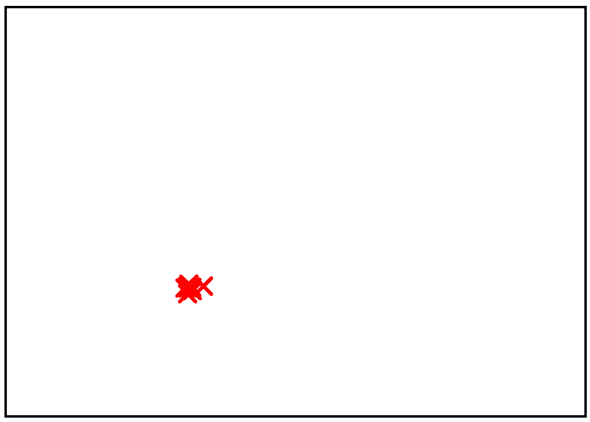

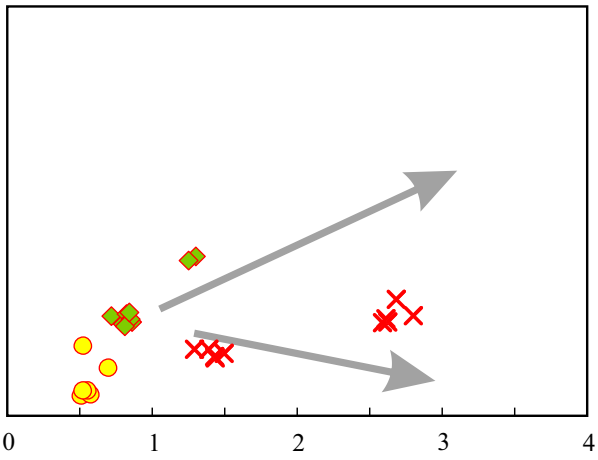

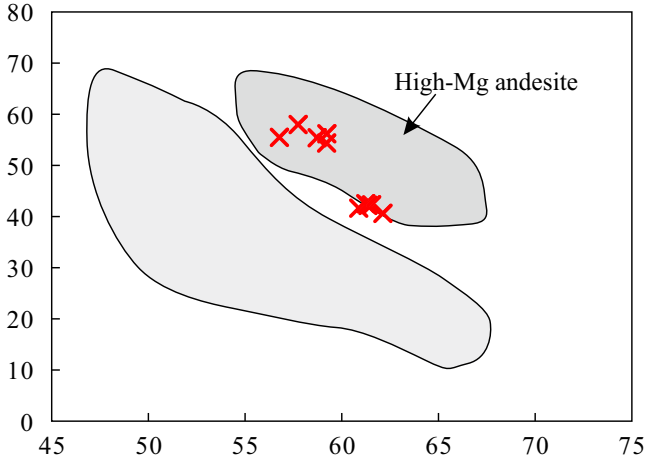

Dawan High-Mg Andesite

Andesite samples display varied levels of SiO_2 (56.8–62.1 wt%), Al_2O_3 (13.9–15.8 wt%), Fe_2O_3 (9.04–11.5 wt%), MgO (3.35–6.30 wt%), TiO_2 (0.61–1.21 wt%), and total alkali ($Na_2O + K_2O$ = 1.52–4.02 wt%). These rocks plot in the field of andesite on the Zr–Ti-Nb–Y diagram (Fig. 9A; Winchester and Floyd, 1977), and they exhibit calc-alkaline trends in the TiO_2-FeO^{total}/MgO diagram (Fig. 9B). Furthermore, they can be classified as high-Mg andesite based on the Mg#-SiO_2 diagram (Fig. 9C).

Despite the observed variation in their REE abundances, all andesite samples display coherent REE patterns (ΣREE = 54.7–114 ppm). Chondrite-normalized REE patterns are markedly LREE-enriched (Fig. 10C), with $(La/Yb)_N$ values ranging from 3.04 to 3.84. They also display significant negative Eu anomalies (δEu = 0.57–0.90) and relatively flat heavy (H) REE patterns (normalized $[Gd/Yb]_N$ = 1.0–1.1; Table 1; Fig. 10C). Normalized to primitive mantle, all samples show variable degrees of depletion in HFSEs, such as Nb (Fig. 10D), thereby sharing an arc-related signature.

Dabanxi Intrusion

Gabbros from the Dabanxi intrusion have SiO_2 contents varying from 46.1 to 48.7 wt%, with relatively high MgO (8.53–12.0 wt%), Al_2O_3 (15.7–19.1 wt%), and TiO_2 (0.90–1.59 wt%) contents, but relatively low levels of total alkalis ($Na_2O + K_2O$ = 2.11–2.98 wt%; Table 1). All samples plot in the subalkaline fields of the TAS diagram (figure not shown) and follow a typical tholeiitic trend in the TiO_2 versus FeO^{total}/MgO diagram (Fig. 9B).

The analyzed gabbros have varied levels of Cr (272–367 ppm), Ni (95–206 ppm), and V (167–260 ppm), with low total REE abundances (30–51 ppm). Chondrite-normalized patterns exhibit slight enrichment of LREEs ($[La/Yb]_N$ = 1.53–1.78) and flat HREE ($[Gd/Yb]_N$ = 1.28–1.42) patterns, with variably positive Eu anomalies (δEu = 1.11–1.31; Fig. 10E). On the primitive mantle–normalized spider diagrams, the gabbros are extremely depleted in Nb, with Nb/La ratios between 0.43 and 0.55, and variably enriched in Sr and Ba relative to their adjacent elements (Fig. 10F), resembling typical continental arc basaltic rocks (Rudnick and Gao, 2003).

Whole-Rock Sr-Nd Isotopic Compositions

Dawan gabbros have varying $^{147}Sm/^{144}Nd$ ratios between 0.2065 and 0.2342, and $^{143}Nd/^{144}Nd$ ratios between 0.512700 and 0.513141, which correspond to a range of initial epsilon Nd (t = 515 Ma) values from +0.6 to +7.4 (Fig. 11). They also show highly varied $^{87}Rb/^{86}Sr$ ratios between 0.0385 and 0.3460 and a relatively large range of $^{87}Sr/^{86}Sr$ ratios from 0.7056 to 0.7078, corresponding to initial $(^{87}Sr/^{86}Sr)_i$ ratios of 0.7046–0.7054 (Table 2). The samples from the Dabanxi intrusion show a narrow range of $^{87}Rb/^{86}Sr$ ratios (0.0932–0.1848) and $^{87}Sr/^{86}Sr$ ratios (0.7070–0.7080), as well as near-identical initial $^{87}Sr/^{86}Sr$ ratios (0.7059–0.7074). The neodymium isotopic compositions of samples from the Dabanxi intrusion have $^{147}Sm/^{144}Nd$ ratios between 0.1792 and 0.1890 and $^{143}Nd/^{144}Nd$ ratios between 0.512626 and 0.512825, with $\varepsilon_{Nd}(t)$ values from +0.6 to +4.1 (Fig. 11). Positive $\varepsilon_{Nd}(t)$ values and low $(^{87}Sr/^{86}Sr)_i$ ratios suggest that the parental magmas of the Dawan and Dabanxi gabbroic intrusions were derived from depleted mantle sources. In contrast to the gabbros, the two representative andesite samples from the lower Lapeiquan Formation have nearly constant initial $^{87}Sr/^{86}Sr$ ratios (0.7117–0.7146) and negative $\varepsilon_{Nd}(t)$ values in the range –3.7 to –5.8 (Fig. 11).

DISCUSSION

Depositional Age of the Lapeiquan Formation

As mentioned above, the ages of one rhyolitic sample from the lower Lapeiquan Formation and two rhyolite samples from the upper Lapeiquan

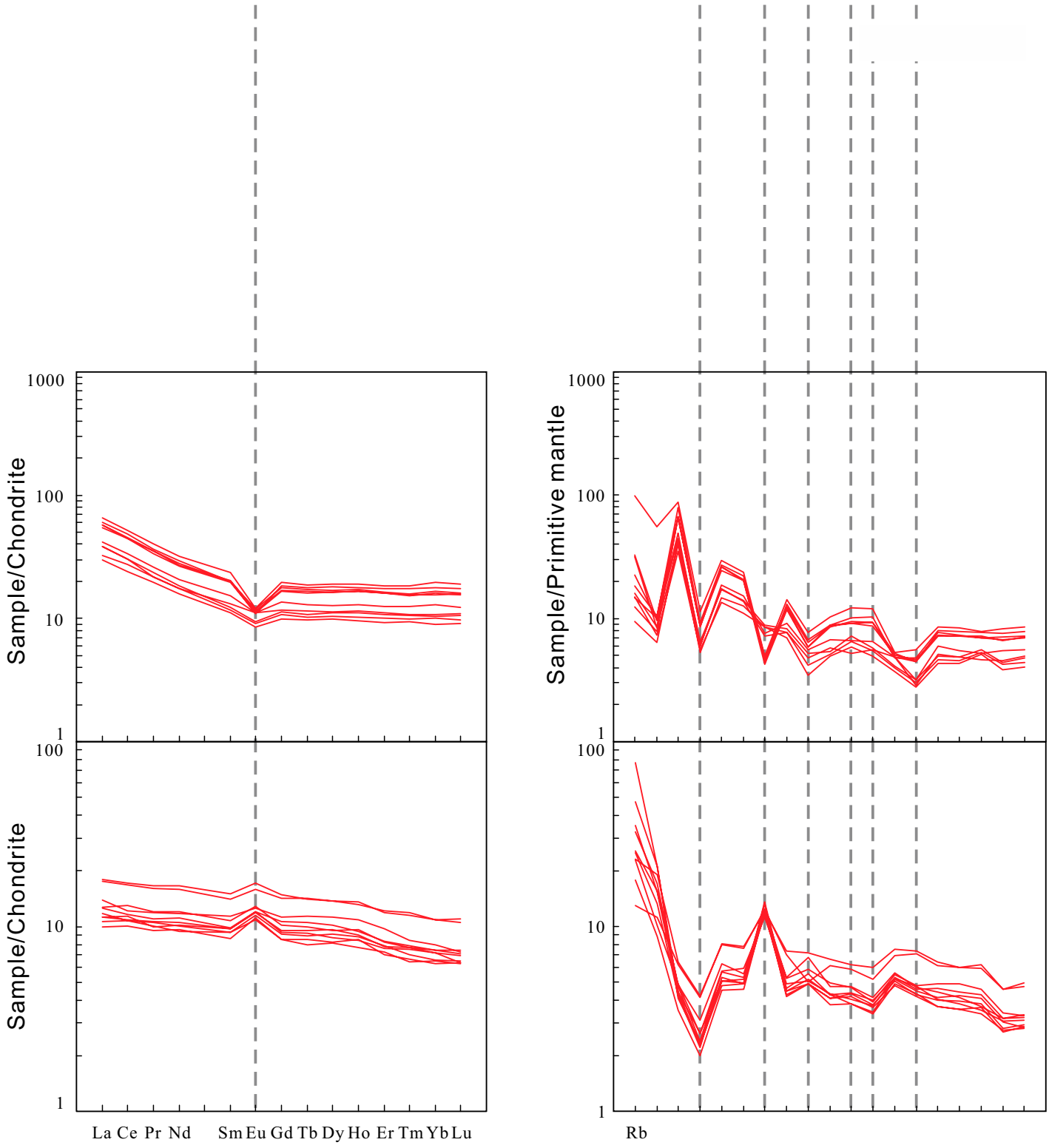
Sample/Chondrite
1000
100
10
1
Sample/Chondrite
100
10
1
La Ce Pr Nd Sm Eu Gd Tb Dy Ho Er Tm Yb Lu
Sample/Primitive mantle
1000
100
10
1
100
10
1
Rb

high-Mg andesites readily rule out the first model. Instead, andesitic melts, which are genetically related to the foundering of mafic lower crust into the underlying asthenospheric mantle followed by immediate partial melting, will produce the depleted signatures (Gao et al., 2004; Qin et al., 2010). Furthermore, partial melting of lower crust generates high-Mg adakitic magma with high Sr (>400 ppm) and Sr/Y (>20), low Y (<18 ppm) and Yb (<1.9 ppm), and high LREE/HREE ratios with $(La/Yb)_N > 20$ (e.g., X.R. Wang et al., 2006; Tang and Wang, 2010; (W)80 (ang, 2010a22 0.0u0ah81to1m65 Tw 0 -1.222ng et al8 (20H0.5 (lo).5 (lv)1in).6 0 (,r

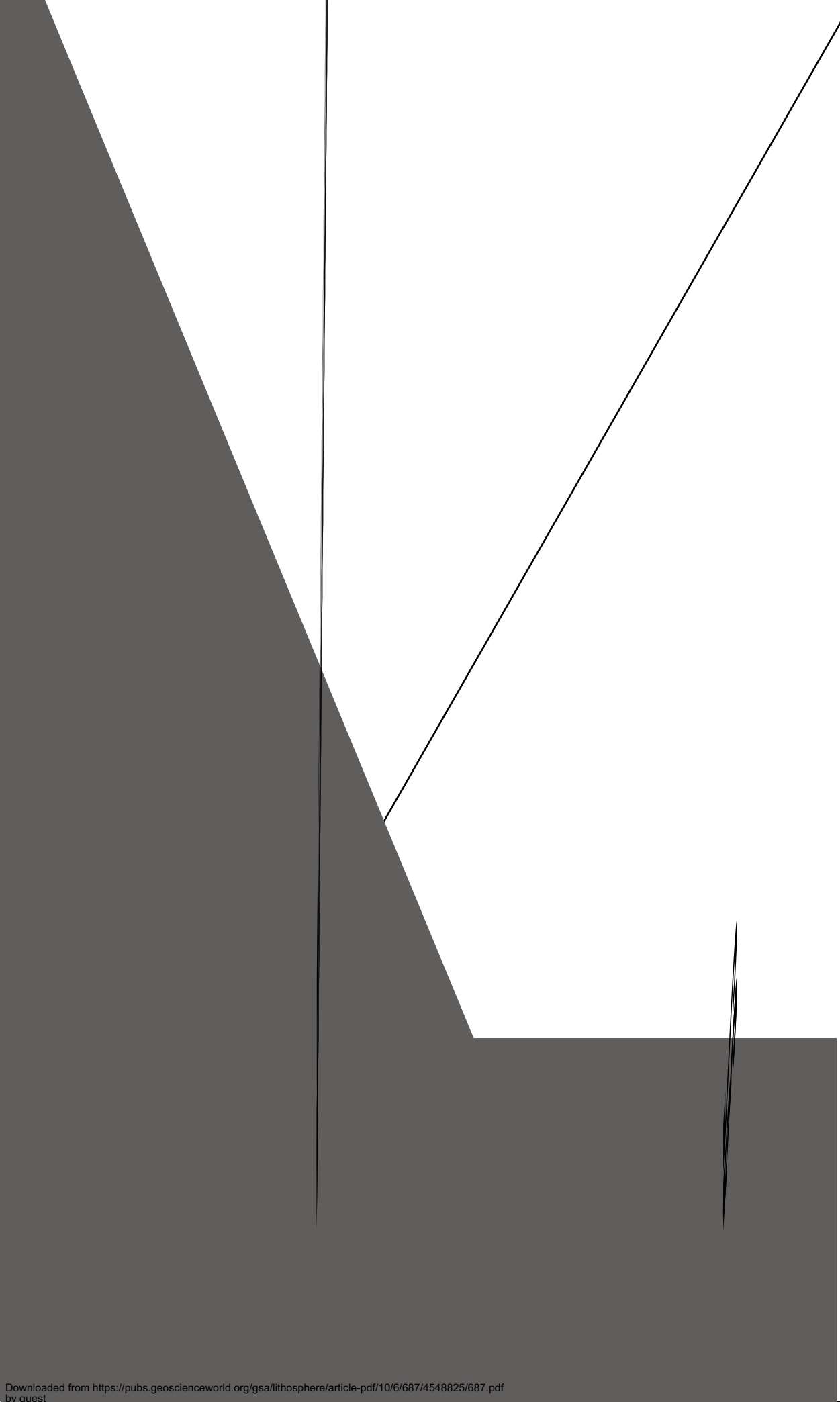

These studies have identified two ophiolite zones (Hongliugou-Lapeiquan and south Altun) in the Altun orogenic belt and have demonstrated the existence of the North and South Altun Oceans (L. Liu et al., 1997, 2012). It is considered that the North Altun Ocean basin opened ca. 750 Ma (H. Liu et al., 2012) and then started to subduct from 520 to 500 Ma (Han et al., 2012; Kang et al., 2011; C. Liu et al., 2016; Wu et al., 2009), and then the subduction angle changed (e.g., slab rollback and flat-slab subduction) during 520–460 Ma, and it was completely closed by ca. 450 Ma (Hao et al., 2006). The existence of volcanic-arc granites on both sides of the Hongliugou-Lapeiquan ophiolite belt suggests that the oceanic lithosphere might have undergone divergent double-sided subduction (C. Liu et al., 2016; J.H. Liu et al., 2017). However, the petrogenesis of the Dawan gabbros and the Dawan high-Mg andesites cannot be sufficiently explained by a normal oceanic subduction event. These rocks were generally related to upwelling of asthenospheric mantle. Three competing mechanisms should be taken into account: (1) ocean-ridge subduction (e.g., Cai et al., 2012; Dickinson and Snyder, 1979; Windley et al., 2007; Sun et al., 2009; Zhang et al., 2014), (2) slab breakoff (e.g., Atherton and Ghani, 2002; Davies and von Blanckenburg, 1995; Niu et al., 2006; van Hunen and Allen, 2011), and (3) slab rollback (Hawkins et al., 1990; Xu et al., 2003; Yan et al., 2016).

Ocean-ridge subduction causes voluminous magmatic activity and HT/LP metamorphism (Kusky et al., 2003; Sisson et al., 2003; Windley et al., 2007). Ridge subduction is responsible for the formation of a slab window, which induces upwelling of hot and depleted asthenospheric mantle. This process generally accounts for the origination of MORB-like adakitic and boninitic rocks (Sisson et al., 2003). Recent studies indicate that the circum-Pacific regions have been affected by ridge subduction in the formation of the accretionary orogens in Japan, Alaska, and Chile (Cai et al., 2012, and references therein). Also, ridge subduction has been invoked in several regions of the Central Asian orogenic belt (e.g., West Junggar, Chinese Altai, and Inner Mongolia; Cai et al., 2012; Geng et al., 2009; Sun et al., 2009). However, the lack of coeval adakites and boninites in the North Altun clearly contradicts the ocean-ridge subduction model. Furthermore, there is no evidence for any high-temperature metamorphic events in this tectonic belt. These findings prompted us to rule out the possibility of ridge subduction during the Cambrian.

Slab breakoff associated with the final detachment of a lithospheric slab (Davies and von Blanckenburg, 1995; Xu et al., 2008) has been proposed as an explanation of the distinct igneous activity during the early stages of continent-continent or continent-arc collision (Atherton and Ghani, 2002; Davies and von Blanckenburg, 1995; Teng et al., 2000; Zhu et al., 2015). However, there is no evidence suggesting the occurrence of early Cambrian (ca. 520 Ma) collision in the North Altun. Instead, the subduction process most likely lasted until ca. 460 Ma in this area (Chen et al., 2016; Cui et al., 2010; Han et al., 2012; S.B. Li et al., 2013; Wu et al., 2016). Thus, the slab breakoff model cannot satisfactorily describe the origin of the Dawan gabbros and the Dawan high-Mg andesites.

Alternatively, it has been suggested that slab rollback played a key role in the generation of these temporally and spatially related igneous rocks. Rollback of the subducting slab would result in extension of the arc lithosphere (Gueguen et al., 1997), which is an important driving force of back-arc basin formation (Nakakuki and Mura, 2013). Partial melting of the upwelling asthenospheric mantle beneath an ocean-ridge system in a suprasubduction zone induces the formation of back-arc basin basalts, most of which show volcanic arc-like and MORB-like compositional characteristics (Evans et al., 1991; Hawkins et al., 1990; Xu et al., 2003).

The Dawan gabbros show varying extents of depletion or enrichment of LREEs and have high $\varepsilon_{Nd}(t)$ values, indicating that a component from depleted asthenospheric mantle was involved in their generation. However, all these gabbros plot between the MORB array and the field of arc-like volcanics (Fig. 14A). Furthermore, the clinopyroxenes from the Dawan gabbros exhibit arc-related trends and plot in the overlapping area between normal MORB and back-arc basin basalt (Figs. 8C and 14B). These observations strongly argue that the Dawan gabbros share a systematic back-arc basin basalt compositional signature and that they were most probably formed in a back-arc basin environment, in apparent consistency with the slab rollback model. In this scenario, the migration of the subducting slab backward into the asthenospheric mantle (rollback) results in the upwelling and decompression melting of hot asthenospheric mantle. This process is followed by partial melting of the subcontinental lithospheric mantle, which ultimately leads to the formation of the parental Dawan gabbro melt. Asthenospheric upwelling results in high-temperature conditions that reheat the cooled subducted slab, subsequently causing sediment melting. These sediment-derived melts react with the mantle wedge and result in partial melting of the metasomatized mantle peridotites, generating magmas like the Dawan high-Mg andesite magmas. Thus, we argue that the slab rollback (formation of back-arc basin) model is also consistent with the formation of the slightly younger Dawan high-Mg andesites.

Previous studies have provided abundant evidence in support of the hypothesis that the North Altun is the western extension of the North Qilian, separated into two parts by the Altyn Tagh fault. Based on identification of a HP/LT metamorphic belt, ophiolites, a subduction-accretion complex, and arc magmatic rocks, the North Altun is considered to be an early Paleozoic accretionary orogen, recognized as the northernmost orogenic collage of the proto-Tethyan domain (Li et al., 2017; Zhang et al., 2015, 2017). The initial rifting of the North Altun Ocean (proto-Tethys) began around ca. 750 Ma, according to the ages of bimodal volcanics identified in the North Altun (H. Liu et al., 2012). Though the exact timing of the initial subduction is unknown, the ocean basin already existed during the early–late Cambrian, as indicated by the ages of the gabbro (480 Ma; Yang et al., 2008) and of the plagiogranite (518–512 Ma; Gai et al., 2015; Gao et al., 2012) from the Hongliugou ophiolitic mélange. From ca. 520 to 495 Ma, oceanic slab rollback induced back-arc extension and resulted in upwelling of the asthenospheric mantle. Dawan gabbro magmas and Dawan high-Mg andesites were generated at the back-arc and the forearc, respectively (Fig. 15A). From the late Cambrian (490 Ma) to the Middle Ordovician (460 Ma), during the subduction of the North Altun Ocean, hydrous fluids released from the slab metasomatized the refractory mantle wedge. The addition of water caused the mantle wedge to be partially melted. Basaltic underplating provided the heat necessary for the melting of the lower and middle crust, which was followed by the generation of arc-related voluminous felsic magmas in the North Altun (Fig. 15B; e.g., Chen et al., 2016; Cui et al., 2010; Han et al., 2012; S.B. Li et al., 2013; Wu et al., 2016).

CONCLUSIONS

(1) Zircon U-Pb dating from rhyolite interbedded in the Lapeiquan Formation shows that the Lapeiquan volcanic-sedimentary sequence was deposited during the late Cambrian (495–485 Ma).

(2) The Dawan gabbro melts were generated from the asthenosphere with variable degrees of contribution from the lithospheric mantle. Dawan high-Mg andesites originated from the subsequent interaction between sediment-derived melts and mantle wedge peridotites. The Dabanxi gabbros were derived from the mantle wedge, which was metasomatized by fluids released from the subducted slab.

(3) The slab rollback model provides a satisfactory explanation of how the Dawan gabbros and the Dawan high-Mg andesites were formed in the North Altun, as the subduction of the North Altun Ocean might have lasted until ca. 460 Ma.

ACKNOWLEDGMENTS

REFERENCES CITED

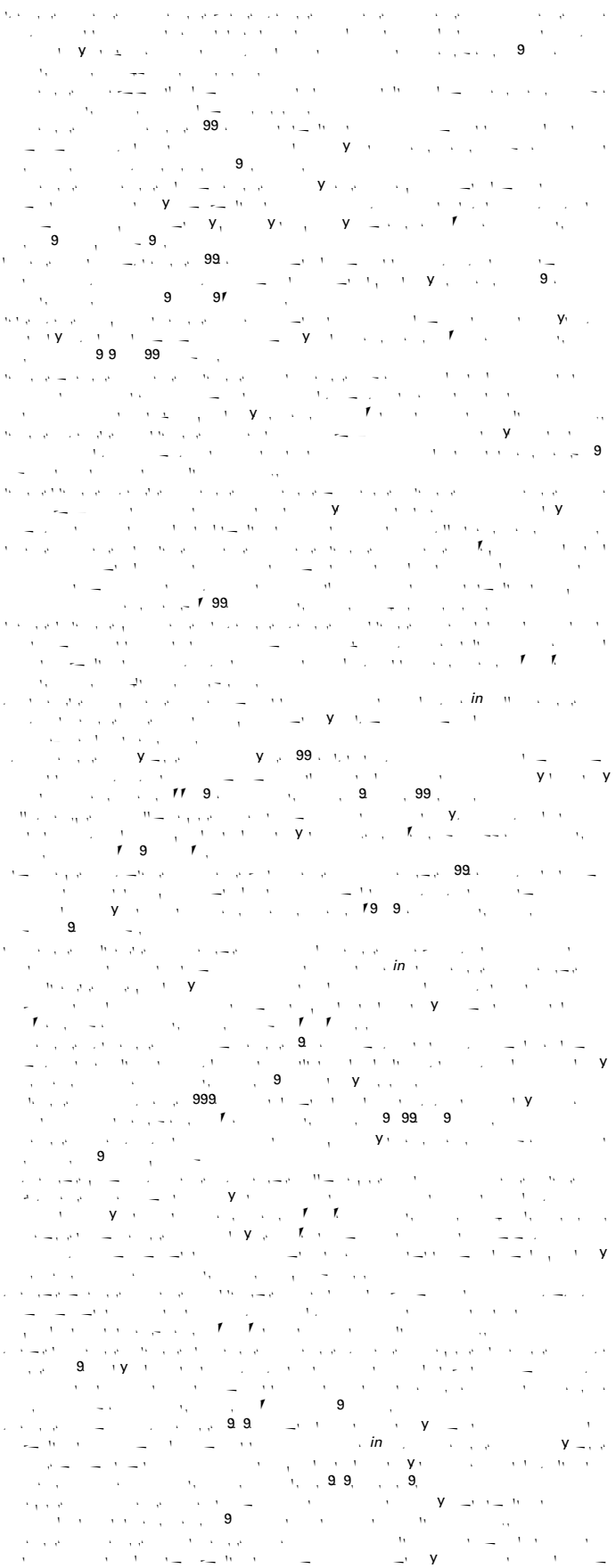

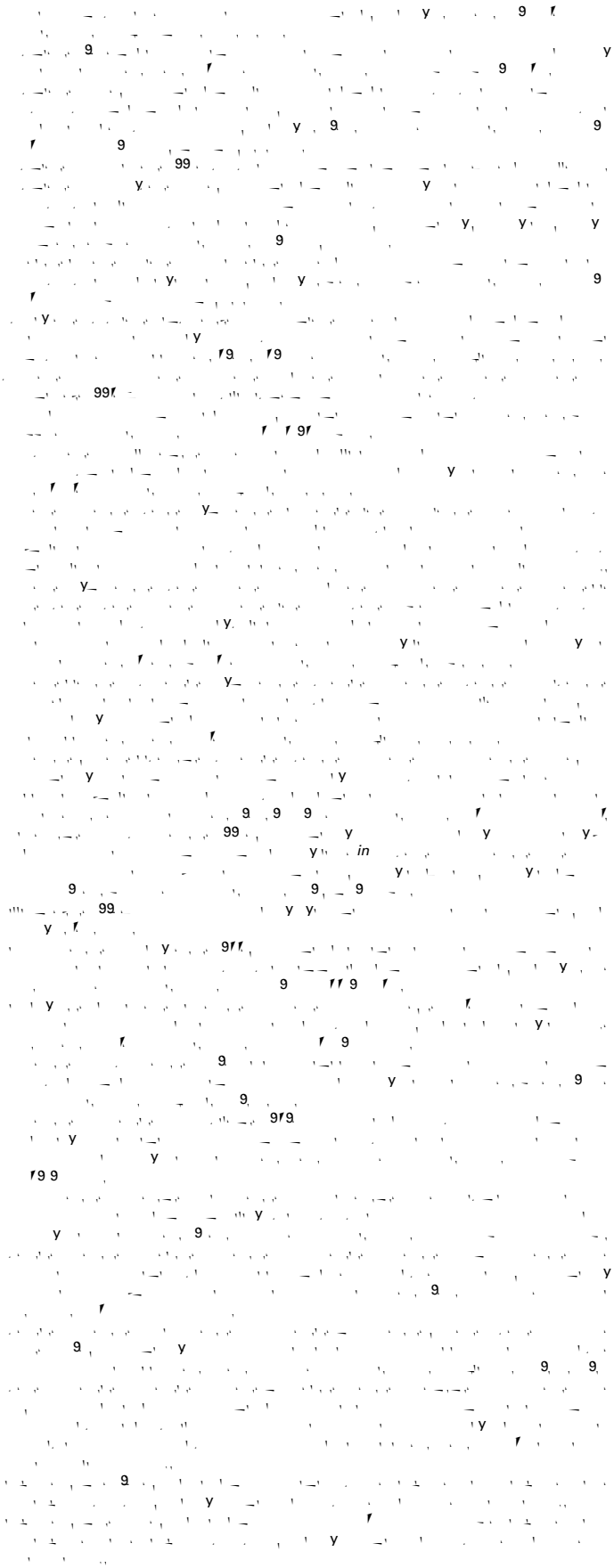

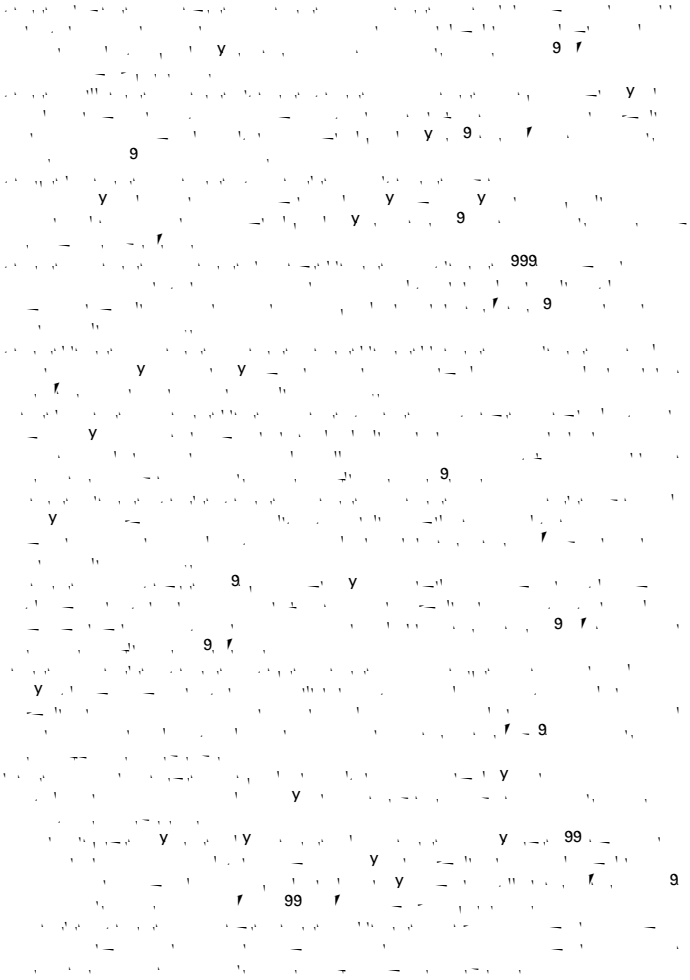

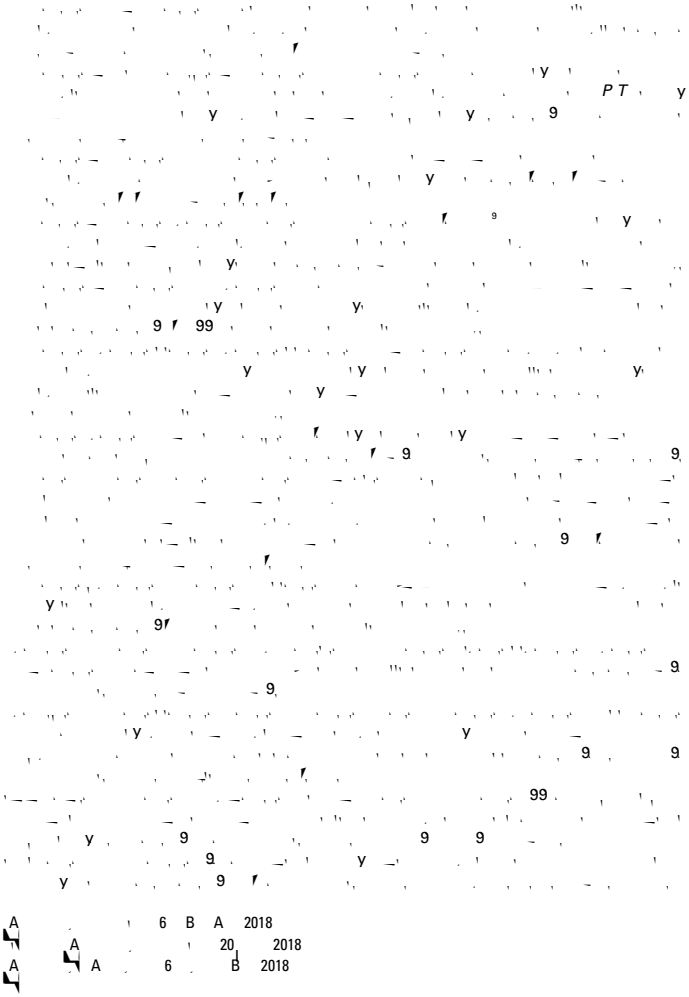

6 B A 2018
20 2018
6 B 2018